OXFORD JOURNAL
OF STUDENT
SCHOLARSHIP

Rotating Rear-Wing Actuation under the 2026 Formula One Technical Regulations: A Parametric Aerodynamic and Vehicle-Dynamic Assessment of the Ferrari SF-26 “Macarena” Concept

Vedant Katira
vedant.katira752@gmail.com

ABSTRACT

The Drag Reduction System was replaced from the 2026 Formula One technical regulations with fully active dual-state aerodynamics, and drivers will be able to choose between a high-downforce cornering mode (Z-mode) or a low-drag straight-line mode (X-mode). The Ferrari SF-26 “Macarena” wing, designed by Ferrari, with its rotating flap as opposed to the traditional hinged flap, and two similar variants created by Red Bull Racing and McLaren are related. This study builds a parametric, physics-based model of this class of mechanisms and tests that model with an aerodynamic model, a quasi-steady lap simulation with the 2026 power-unit deployment taper and a brake-application stability model, all of which are proprietary. Assumptions are presented as parameters and propagated through Monte Carlo analysis.

Three findings emerge. First, a 180° inversion is aerodynamically inferior to a conventional X-mode flap (−20.7% versus −22.3%), and reduces the rear-wing loading to −30 % of its Z-mode value, while shifting the aerodynamic balance to 88.9 % up front. The drag reduction is greatest around 270°, when the chord is aligned with the freestream and the gap between the chord and the freestream is open, with a drag reduction of −26.2% at this point. The model predicts a relatively small advantage over a conventional X-mode flap, approximately 0.28 s at Spa-Francorchamps, 0.18 s at Silverstone, 0.12 s at Circuit Gilles-Villeneuve, 0.10 s at the Hungaroring, and less than 0.01 s at Monaco. Monte Carlo uncertainty propagation gives an estimated Spa advantage of −0.276 s [95% interval: −0.363 to −0.201 s] and a Hungaroring advantage of −0.100 s [−0.132 to −0.074 s], indicating that the direction of the predicted benefit is robust but its precise magnitude remains uncertain.

Third, the time to recover from downforce is a primary safety concern: recovery time increases by only 8 – 17ms per lap when made 500ms compared to 100ms, and the modelled probability of having the rear axles saturated during braking is raised from below 1% to 57% in line with the FIA's 400ms recovery limit. In general, the results demonstrate that the rotating-flap concept is only of modest benefit in terms of performance, but that the aerodynamic recovery properties are essential to ensuring braking stability and safety in the context of the 2026 active-aerodynamics regulations.

***Keywords*:** Formula One; active aerodynamics; 2026 technical regulations; rotating rear wing; X-mode; flow separation; vehicle stability; lap time simulation

1. INTRODUCTION

The new 2026 Formula One World Championship will feature some of the biggest packages of technical regulation changes in modern Formula One history. The first use of aerodynamic wings in Formula One was in 1968 when they were inverted for the purpose of creating vertical load and enhancing tyre traction. Since then, aerodynamic regulation has evolved with the multi-element high downforce designs of the 1990s/2000s, the adoption of the Drag Reduction System and the resurgence of ground-effect-dominated vehicle concepts in 2022. Today in Formula One cars, aerodynamic loading directly affects cornering ability, braking stability, straight line performance, and vehicle balance (Katz 2006; 2019).

New active aerodynamic systems and a significantly modified hybrid powertrain are added to the 2026 regulations. The electrical power contribution to propulsion is increased, which is a key limitation on long straights. To minimize drag as appropriate, the regulations include aerodynamic operating states which are coordinated: Z-mode for high downforce and X-mode for lower drag. The front and rear aerodynamics are therefore not static aerodynamic surfaces, but rather dynamic parts of the vehicle's performance. (Federation Internationale de l'Automobile 2026c).

The implementation of these rules in a more controversial fashion is the rotating rear wing on the Ferrari SF-26. In what is a relatively new idea, Ferrari designed something that pivots through a wide angle instead of pitching through a small one, with compact actuators in the endplates of the rear wing. The device was first tested at Bahrain pre-season and was modified after the Chinese Grand Prix due to some delays in closing, and has been a permanent addition since the Miami Grand Prix. A higher downforce version was introduced at the Hungarian Grand Prix. Red Bull Racing and McLaren developed their own ideas of rotating flaps, with both retaining the centrally mounted actuator, but not the installation of the endplate.

It is proposed that this will result in a large rotation reducing the surface pressure differential across the rear wing to a greater extent than a hinged flap, and thereby create rear-wing and diffuser load that is meant to be cancelled out. The effect is dynamic: the bigger the angular travel (and hence longer the time taken to return to the high downforce configuration), the longer the vehicle will have a forward-shifted centre of pressure and the longer it will spend with a critically unloaded rear axle (Soso and Wilson 2006; Ehirim et al. 2018).

This paper queries whether the rotating mechanism will enhance the straight-line velocity, aerodynamics and lap performance within the 2026 regulations and how much it will affect the stability of the car that it rides on. The pertinent proprietary data are not available to the public, so this question is raised by declaring a parametric model and establishing predictions in a way that wind tunnel or computational analysis may disprove.

1.1 Data provenance and epistemic status

It is essential to present a statement at the beginning of this investigation clarifying what it claims and what it does not claim, because the quantities in the secondary literature with regard to this device cannot have been measured by anybody outside the teams involved in the investigation. The per-session drag coefficient reduction, rear-axle residual downforce fraction and actuator recovery time are internal computational and simulator outputs. They are not produced or recorded by teams; they are not in FIA files, and they are not available via timing or telemetry. Numbers like this in technical comments, such as a drag reduction of a constant –34 % on circuits that are very different in terms of their rear wing specification, are not physically plausible, as teams alter their rear wing substantially between low-downforce and high-downforce circuits.

2. FUNDAMENTALS OF FORMULA ONE AERODYNAMICS

2.1 Aerodynamic forces

The goal of modern Formula One aerodynamics is to generate as much vertical downward force as possible, but with as little drag as possible. They both come from the integration of surface pressure and shear stress over the body of the vehicle, and both are expressed in non-dimensional form (Katz 2006; 2019):

The quadratic nature of downforce means that high-speed cornering stability is achieved by maintaining a high C□, and on straights terminal velocity is degraded by the same quadratic term, as induced drag and parasitic drag. For this paper, the coefficients are reported in terms of area, C_LA and C_DA, a convention used in vehicle aerodynamics, and eliminating an arbitrary reference area.

$F_L = ½ \rho v^2 S C_L$

$F_D = ½ \rho v^2 S C_D$

- F_L is aerodynamic lift force, with negative lift corresponding to downforce in the vehicle convention used in this study;
- F_D is aerodynamic drag force
- ρ is air density;
- v is freestream velocity;
- S is the reference planform area;
- C_L is the lift coefficient;
- C_D is the drag coefficient.

The ratio C_L/C_D provides a conventional measure of aerodynamic efficiency, although the present analysis primarily reports C_LA and C_DA to avoid dependence on an arbitrarily selected reference area.

2.2 Ground effect

In the current formula, underbody aerodynamics use ground effect (as a Venturi duct). It follows from continuity and Bernoulli's equation: a narrowing of the flow path means that velocity increases and static pressure decreases (Zhang et al. 2006; Zhou et al. 2026).

$$A_1 v_1 = A_2 v_2 \qquad p_1 + \tfrac{1}{2}\rho v_1^2 = p_2 + \tfrac{1}{2}\rho v_2^2$$

Air that gets under the front splitter is accelerated through the constriction under the sidepods, creating a low-pressure area under the centre of gravity that pulls the chassis to the track. The performance of this system is heavily dependent upon conditions at the back of the car – the rear wing creates an upwash which acts as an extraction pump, pumping mass flow out of the diffuser, and increasing underbody load. The present study deals with this coupling as it is central to the entire device; the reduction in drag and loss of downforce caused by stalling the rear wing also applies to the diffuser, and these two are not treated separately.

2.3 Wake structures and vortices

The control of air that moves out of the vehicle is as important as the control of air that moves into the vehicle. The flow close to the tips of a wing is caused by pressure difference and produces energetic tip vortices. Prior to 2022, deliberate formation of such structures was allowed, most notably the Y250 "vortex" at the intersection of the required neutral front wing centre section and the outer flaps, which facilitated closure of the sides of the floor from lateral pressure entry. The current regulations have been modified to remove the Y250 and require continuous curved front wing profiles to merge with the crash structure (Katz and Dykstra 1992; Lau and Srigrarom 2010).

Wake mitigation and upwash management is thus the new focus of vortex control. The rear endplates and diffuser work together to 'fling' the combined wake up to the following car, and the front wing endplates help to push the tyre wake away from the floor endplates. The 2026 rules changed this rear upwash structure from being static to being a many-times repeated switch-on and switch-off, a qualitatively new situation for the car creating the upwash as well as for the car following (Guerrero and Castilla 2020).

3. EVOLUTION OF FORMULA ONE WING DESIGN

3.1 Early wing concepts (1968–1980)

Aerodynamic downforce appeared in Formula One in 1968, bringing a new era that culminated in a new shape that resembled a 'cigar'.Taking inspiration from the technologies used in the aerospace industry, Ferrari and Brabham attached aerofoils straight to the uprights of the suspension on thin struts, high above the chassis in clean air. The uprights were used in the routing so as to avoid the springs and to increase the grip a lot (Wright 1982).

These structures were not stiff enough, nor made of a strong enough material to resist the load they produced and aeroelastic flutter and outright failure occurred frequently. Following several serious crashes at the 1969 Spanish Grand Prix, the FIA decided to outlaw high-mounted strut set-ups and to make all aerodynamic surfaces rigidly mounted within a certain range under the sprung mass. The attention then turned to integrated flow management in the 1970s, with the inverted aerofoil shape of the

car's sidepods and the sliding skirts that were used to seal the perimeter around the car. The focus then shifted to integrated flow management, culminating in the Lotus 78 and 79 ground-effect cars, which featured a sculpted aerofoil shape inverted on the bottom of the sidepods, and sliding skirts that closed the perimeter around the bottom of the car. The result was a decrease in the use of conventional wings, until the FIA banned the use of the technology after 1980 for safety reasons (Katz 2019).

3.2 The high-downforce era (1990–2010)

After the full-length skirts were banned and the flat bottoms of the 1983 legislation, multi-element upper bodywork was developed. The rear wings evolved into a series of slotted flaps in cascade attached to a mainplane. They rely on the slot-gap effect, a pressure surface high-energy flow bleeding into the boundary layer of the next body, re-energising it and thus resulting in a delay of separation at high angles of attack. The mechanism is directly applicable to the present study since the idea of rotating flap is to deliberately destroy it (Castro and Rana 2020).

By the mid-2000s, the aerodynamic shape had become all but unrecognisable with localised devices all around the chassis. These created a wake which had a much higher turbulence level, but also a low total pressure, that caused the front wing of any subsequent car to stall, thus limiting overtaking. The FIA reacted to the situation by introducing a new regulation that was released in 2009, which was designed to make bodywork easier to wind and to clear the wake (Guerrero and Castilla 2020; Katz and Dykstra 1992).

3.3 Complex multi-element wings (2010–2021)

The 2009 rules were not that simplistic; they were more about the point than about thumping the air in the other direction. They placed aerodynamics in the direction of vortex manipulation. The gap between the required 250 mm neutral front wing centre section and the sculpted outer aerofoils was used to create the Y250 vortex that was optimised to flow away from the front tyres and effect a virtual skirt that enclosed the underfloor low-pressure area (Buscariolo et al. 2022; Lau and Srigrarom 2010).

In 2011, Active aerodynamics hit the sport in the form of the Drag Reduction System, which opened a set slot (up to 85mm) in the upper wing of the rear wing, thus lowering drag during overtaking manoeuvres. At the same time, teams were working on passive aeroelastic tailoring, placing composite structures so that when they were most dynamic, under peak drag conditions, the elements would deflect backwards to absorb drag, but when loads decreased before braking, the elements would return to their high downforce configuration. The present analysis can be used as a useful reference for this passive flexure since the recovery time is zero, since the geometry is a direct function of the aerodynamic loading and so is not a factor to be designed intentionally, as it would be to be a factor in an actuated rotating mechanism.

3.4 Ground-effect regulations (2022–2025)

In 2022, rules took the upper-body vortex dependency and replaced it with the underbody ground effect. Clean swept wing profiles were required to integrate into the nose of the aircraft, and wing end plates were rounded into smooth upsets to reduce tip vortices and direct the wake up into a narrow raised upwash. Wake sensitivity decreased, but the use of low-riding floor geometry led to very strong aeroelastic (porpoising) instability, where the car gets very close to the ground, and the suction on the

floor is not strong enough to stop the flow from being choked; the car bounces back up, and the process repeats. The car had to be low and stiff to be stable with static wings, but to ride and be mechanically compliant was a significant sacrifice (Nebot et al. 2025).

3.5 Active aerodynamics and the 2026 framework

The 2026 rules completely de-emphasize static aerodynamic configurations. With today's power delivery qualities of the new hybrid power units and the resulting straight-line energy clipping, passive drag profiles are not realistic anymore. DRS is superseded by a dual-shaft synchronised control method which involves active, moving adjustment at both ends with a multi-element front flap system. Teams are switched from Z-mode to X-mode as needed (Federation Internationale de l'Automobile 2026c).

The rotating idea takes the element through a large angle of flap incidence when conventional interpretations only have a limited range of angles. The promised effect is that the mechanism does not even come into contact with the restriction of the gap adjustment in the slot. Section 4 discusses what such a mechanism would actually be doing aerodynamically, and Section 7 quantifies the value of such a mechanism.

4. AERODYNAMIC CHARACTERISTICS OF THE ROTATING WING

4.1 Design objectives

The idea is to tackle four coupled goals: create high cornering downforce, a large drag reduction on straights, control the downstream flow field, and control the transient position of the centre of pressure during mode changes. In Z-mode, the wing functions as a standard, highly cambered multi-element assembly which gives the vertical load that controls braking and cornering stability.

This is not the case in X-mode. The element does not move in a small arc but rotates in a large one, and the drag reduction is coupled with the underbody: When the rear wing is unloaded, the diffuser will shed load in sync with it, and it ceases to have an extraction pump function. The design intent is that this is done symmetrically enough to keep the "corners in balance" during transitions, which is tested by this study (Chatpattanasiri et al. 2022).

4.2 Geometric parameters

The parameters controlled by actuators in the endplate assemblies affect performance. These descriptors are (Laguna-Canales et al. 2023; Castro and Rana 2020):

- Camber distribution: High camber (Z-mode) to maximise flow turning. Camber for a large rotation is opposite the freestream.
- Chord length and chord ratio: The distance between the mainplane and the secondary element; the ratio is the chord ratio and determines slot energisation.
- Angle of attack: in Z-mode, the element is running at its functional limit, but before separation. Its rotation takes it through 0° (no rotation) and to 180° (reversed).
- Endplate geometry: endplates are used structurally as housings for the actuators, but also as aerodynamic sealing to reduce the strength of induced tip vortices and lateral pressure spill.

The state of the wing is not reduced to the angle of rotation but to two independent parameters, the chord-line incidence α and the slot gap ratio g/c, in the model developed here. The separation is crucial. A conventional flap will have a low incidence but will still be close to the mainplane; therefore, g/c will remain at a moderate level. This rotating flap is able to reach a low incidence and pass entirely under the mainplane, hence the large value of g/c. If both mechanisms involved in the collapse were studied together, the study would be assuming the conclusion.

4.3 Flow control mechanisms

In Z-mode, the assembly is attached through the normal flow attachment, with the slot introducing high-energy flow into the boundary layer of the downstream element, which maintains attachment under an adverse pressure gradient, and with the sharp downstream edge creating the upwash, which provides the extraction force for the diffuser.

While the element is rotating, there are two things happening. As the slot gap increases, the flap has less effect on the mainplane, until the mainplane completely frees itself from the flap. By itself, the element's incidence drops to zero, then it becomes negative as it continues to rotate, with the camber also being inverted. These two effects occur at different times and intensities, depending on the timing of the other, which determines the aerodynamic state; Section 7 demonstrates that they do not occur simultaneously at their optimum rotation angle (Soso and Wilson 2006; Buscariolo et al. 2022).

A common claim is in error. The inverted tyres are also claimed to provide beneficial positive lift which helps to unload the rear tyres and lowers rolling resistance. It shows here that an inverted cambered section at significant negative incidence is a bluff body, and indeed it does generate a net upward force; but not at low-pressure drag – it does it at high-pressure drag, and that is a problem when it comes to braking, not the straight. The quantitative examination is done in Sections 7.1 and 7.5.

The idea is also sensitive to transient timing. If the rear wing's recovery is slower than the front wing's flap recovery, then the centre of pressure moves forward through the plane, and the rear axle is prematurely unloaded. In Section 6.3 this is codified into a measure of stability margin, and in Section 7.5 the associated risk is quantified.

5. COMPUTATIONAL FLUID DYNAMICS APPROACHES

5.1 CFD workflow

To evaluate the transient performance of a rotating rear-wing element, a computational tool that supports moving geometry is needed. Before the geometry is simplified, fasteners, non-structural gaps and internal cavities that don't contribute to the external flow should be removed. It is then possible to parameterize the wing at a number of rotational positions between 0-270°. There should be adequate near-wall and wake resolution, and the computational domain should be large enough to capture the effects of the boundary-layer, separation, and interaction of the rear wing and diffuser. Boundary conditions are:

- Uniform or profile-corrected freestream at the inlet (low-speed corner entry to terminal straight-line velocity of 100 m/s).

- To correctly simulate the ground-effect extraction, a moving ground wall with inlet velocity translation and rotating wall conditions on the wheels were used.
- Pressure outlet: 0 Pa gauge, allowing it to flow out freely.

The pressure-based coupled transient solver is used to solve the moving parts. Both qualitative topology (streamline/ isosurface visualisation) and quantitative force and surface pressure coefficient data are extracted as part of the post-processing.

Aerodynamic reattachment does not always happen as the inverse of aerodynamic separation, which is why the transient closure is of particular importance. It takes a certain time to restore downforce, which is dependent on the speed of the actuators, the aerodynamic loading of the moving flap, and the flow-reattachment hysteresis. The aerodynamic endpoints can be estimated in a quasi-static sequence but it is not possible to directly resolve the transient recovery process. A moving-mesh or overset (moving) transient CFD simulation would thus be most useful in the future for validating the assumptions made for the recovery time in the present model. (Spalart et al. 1997; Menter 1994).

5.2 Turbulence models

Important here is the model selection since the whole concept is developed under the massively separated flow conditions where the use of eddy-viscosity closures is least reliable.

- k-ε: good and cheap in free-shear regions, not so good in adverse pressure gradients and not so good in separating onset. Not suitable as a first line of defence in solving this issue.
- k-ω SST: standard industrial model, a mix of k-ω near the walls and k-ε in the freestream. Allows for a reasonable prediction of when separation will occur but is not always the best predictor when stall has set in.
- LES: Solves the energetic scales directly and includes wake unsteadiness, at unaffordable prices for a full vehicle at racing Reynolds numbers.
- Hybrid RANS/LES: RANS in attached regions, LES in separated regions. The right balance in the case of a stalled wing assembly, and the preferred method for testing the drag values given in Section 7.

5.3 Meshing strategies

Structured hexahedral meshes are found to be superior in accuracy per cell and the numerical behaviour in boundary layers; however, they are impractical to generate around the complex multi-element geometry with moving parts. In practice, unstructured or poly-hexcore meshes are used as a standard solution, with prismatic inflation layers in the near-wall region where they are required to be spaced close to the wall in accordance with the wall treatment. If any parts are rotating, there must be either sliding interfaces or an overset arrangement to ensure that the moving parts do not affect the quality of the cells during rotation. Since the resolution requirements are quite different in the two states, Mesh independence needs to be verified separately for the attached Z-mode state and the separated X-mode state.

5.4 Validation methods

The computational results must be compared with wind tunnel results obtained at matched Reynolds number if possible, taking into account the effects of blockage and scale. The surface pressure and particle image velocimetry measurements are used to provide a field-level comparison, to validate that, rather than merely proper integrated force, the correct flow topology has been reproduced. If a device is currently transitioning, then the transient needs to be included in the validation: If it mispredicts the endpoint states, it would leave the stability question unanswered (Mariani et al. 2015).

6. METHODS

6.1 Aerodynamic model

The incidence of the chord line of the flap is controlled by rotating the flap and is represented as a single element. Due to the fact that the element is far outside the attached flow, it is necessary to use a blended closure. If thin-aerofoil theory were used, in the attached branch with a finite-span correction according to Prandtl's lifting-line theory, one would obtain (Katz and Dykstra 1992; Lau and Srigrarom 2010):

$$C_L\, C_{L^0} + [a_0 / (1 + a_0/\pi eAR)]\, \alpha, \quad C_d = C_{d_0} + C_L{}^2/\pi eAR, \quad a_0 = 2\pi$$

For the fully separated branch, the standard closure for high-incidence aerodynamics is used, that is, the Hoerner flat-plate normal force model (Katz 2006; 2019).

$$C_N = 2 \sin\alpha / (0.222 + 0.283/|\sin\alpha|), \quad C_L = C_N \cos\alpha, \quad C_d = |C_N \sin\alpha| + C_{d_0}$$

The branches are mixed according to a logistic weighting centred around the static stall incidence, resulting in a continuous polar over the entire range of rotation (Figure 1).

There are three geometric quantities that are driven by rotation. Chord-line incidence is expressed as $\alpha(\theta) = \alpha_Z \cos\theta$; camber orientation is expressed by the sign of $\cos\theta$; and the gap ratio of the slot increases monotonically, with a maximum at 180° and is open after the same angle, since the flap has cleared the mainplane wake. This kinematic mapping is assumed, not measured and thus scales with this assumption. There are three geometric quantities which are due to rotation. Chord-line incidence is shown as $\alpha(\theta) = \alpha_Z \cos\theta$; the camber orientation varies with the sign of $\cos\theta$. As the rotating flap is swung away from the mainplane the slot gap ratio g/c increases to the assumed fully open value of 0.62 when the flap is approximately 180°. This maximum value of g/c is maintained for the simplified kinematic model presented here, as the flap continues to turn towards a near-streamwise orientation, from 180° to 270°. Therefore, the gap ratio modelled in the two situations (180° and 270°) is the same, but the modelling of the chord-line incidence is significantly different. This kinematic mapping is an assumed model input and should be considered as a parametric mapping and not as a measured Ferrari geometry.

Mainplane circulation is maintained by slot pumping, and rapidly decreases with gap (Soso and Wilson 2006; Buscariolo et al. 2022).

- $\eta_{main} = exp[-k(g/c - g_0/c)]$
- $C_{D,main}\, Z = F_{stall} + (1 - f_{stall}) \cdot \eta_{main}{}^{1.5}$

In this case, the factor f_{stall} = 0.34 is the pressure drag around the bluff body of a mainplane that has stalled. The inclusion of this term is essential, and the lack of this term is the probable source of the very large drag reductions as reported in secondary sources, which are only for the lift-dependent component of drag, not the pressure drag. This is about double the predicted benefit if this term is not added. Sensitivity analysis in Section 7.6 says that it is the most important uncertainty in the study.

$$C_L = C_{L0} [a_0 / (1 + (a_0 / \pi eAR))] \alpha$$

$$C_D = C_{D0} + (C_L^2 / \pi eAR)$$

$$a_0 = 2\pi$$

- e is the span-efficiency factor.
- AR is the aspect ratio.
- C_{L0} is the lift coefficient at zero-incidence.
- C_{D0} is the drag coefficient at zero-incidence.

$$C_N = 2\sin\alpha / (0.222 + (0.283 / | \sin\alpha |))$$

$$C_L = C_N \cos\alpha$$

$$C_D = | C_N \sin\alpha | + C_{D0}$$

- C_N for normal-force coefficient
- C_{L0} and C_{D0} for zero-incidence/reference coefficients

6.2 Vehicle and lap simulation

A quasi-steady point-mass simulator is used and is based on a 1m spatial grid. Grip-limited apex speeds are computed explicitly because downforce is proportional to v^2; a forward pass puts a traction/power limitation, a backwards pass puts a braking limitation, the velocity profile is the pointwise minimum and lap time is the result of the integration of ds/v.

The power unit is estimated to be around 400 kW thermal and 350 kW electrical, and the regulatory deployment taper will reduce the power of MGU-K from full power at 290 km/h to nothing at 345 km/h. To date, there has been no car with this coupling to refer to; this is significant to the outcome: the lower-drag car comes into the tapered zone sooner, and thus part of the benefit of the aerodynamic benefit is lost due to reduced electrical deployment. Any analysis which considers the 2026 low-drag benefit as being the same as a DRS benefit will overestimate it (Federation Internationale de l'Automobile 2026c).

The sections are represented by five circuits as simplified sequences of straight sections, which have been scaled to the official lap distance (Table 2). Absolute lap times are within about 5-9 % of real 2026 times, and these are not adjusted any further; the number reported everywhere is the difference between the times of two different configurations and is much less affected by layout detail than absolute time.

6.3 Stability model

It would be intuitive for a slow-recovering wing to fail at the corners, but, at low speed, in a plane with low dynamic pressure, the loss of downforce due to failure of the corners is virtually inconsequential. The critical instant is at the end of the straight, at 300- 350 km/h, when the rear axle has the maximum amount of grip to be aerodynamic.

The driver and the brake-by-wire calibration team agree on the deceleration the recovered car can achieve: a_x = μ(mg + qC□A_recovered)/m, where the capacity is calculated using the actual load, which is partially recovered, at the rear of the car: qC_LA_recovered.

$$N_r = mg \cdot k_r - m \cdot a_x \cdot h/L + q \cdot C_LA\ rear(t)$$

$$SM = \mu N_r / \sqrt{(F_x,r^2 + F_y,r^2)}$$

If SM < 1, it means that the rear axles are saturated. Downforce restoration is assumed to be a 1st-order lag, and to be 95 % recovered after t = τ. But a driver has to anticipate by picking up the closing time before they need to brake, and this has its limitations: If they anticipate too early, then they miss the low-drag benefit of the fastest part of the lap over v·t_budget metres. It is assumed that the budget is 0.25 s. With a τ below that amount, it's fairly safe. With a τ above that, it's at the braking point even when the driver takes their foot off the gas. We model the actuations as a log-normal perturbation with an additive term, allowing us to assess the possibility of P(SM<1).

6.4 Experimental methods for validation

Facilities and instrumentation must be provided for testing an active mechanism that are not available for static bodywork. The FIA requirements demand that the testing be done with 60 % scale models and for this device, the internal actuators need to produce the full rotation during each test and not be fixed between tests. In order to have the correct underbody extraction caused by the rear wing, a rolling road synchronised to the freestream will be needed.

Multi-axis internal balances isolate vertical load, drag and lateral moments and are used to mount the models. In the case of transient work, the sampling rate is the limiting factor; it takes at least a sampling rate of 1 kHz to resolve a 200 ms recovery event, and the amount of interest is the force time history, not the endpoint values (Buscariolo et al. 2022; Mariani et al. 2015).

Flow visualisation data is complementary to integrated force data. The smoke visualisation is used to determine gross streamline topology and the wake structure. Using a laser sheet and high-speed cameras, particle image velocimetry is used to illuminate oil mist particles in the domain and capture the velocity fields, giving quantitative velocity fields and vortex core structure. Pressure-sensitive paint (PSP) can be used to map the surface pressure across a surface continuously and thus is useful in determining whether flow has reattached or remained separated over the reversed flap. The question of whether a flow is

reattached or separated along a reversed surface is answered with PSp by making continuous surface pressure mapping, which is the most direct method of determining reattachment.

Aeroelastic deflection and mechanical reliability are covered in structural testing. Static load rigs are used to implement the FIA deflection envelope. The digital image correlation method in the tunnel is used to observe the deformation and confirm that there is no jamming or fluttering phenomenon under the action of dynamic load. For this concept, an additional requirement is endurance – a mechanism that performs a large amount of angular motion many times per lap will also have a high number of actuator duty cycles compared to one with a hinged flap, and actuator recovery time degradation due to wear is directly related to safety; refer to Section 7.5 for the threshold behaviour reported.

7. PERFORMANCE ANALYSIS OF THE ROTATING WING

7.1 Downforce generation and the rotation optimum

Table 1 reports the modelled aerodynamic state of each configuration. The comparison is against a Z-mode baseline of C□A = 3.50 m² and C_DA = 1.02 m².

Configuration	α (°)	g/c	C□A (m²)	C_DA (m²)	ΔC_D (%)	Rear residual (%)
Z-mode baseline	28.0	0.03	3.50	1.020	—	100.0
Conventional X-mode	3.0	0.30	2.87	0.793	−22.3	53.6
Rotating flap, 180°	−28.0	0.62	1.73	0.808	−20.7	−29.5
Rotating flap, 270°	0.0	0.62	2.58	0.752	−26.2	32.8

Table 1. Modelled whole-car aerodynamic states. The 180° configuration delivers a smaller drag reduction than a conventional flap while driving the residual rear-wing load negative.

The main conclusion is that a 180° inversion is a poorly aerodynamically designed flap compared to a traditional X-mode flap. It is fully inverted at 180° incidence at −28° incidence and mimics a bluff body, with the net upward force causing the residual rear load to drop to −29.5 % aerodynamic balance shift towards the front, to 88.9 % compared to 44.0 % for the conventional flap it aims to outperform, and a smaller drag reduction (−20.7 %) than the conventional flap (−22.3 %).

The benefit is at the angle of about 270°, where the chord is again parallel to the freestream, and the slot gap is completely open. The value of drag reduction is −26.2 % with a small positive rear load. The minimum drag is at about 250°, not 180° (see Figure 1).

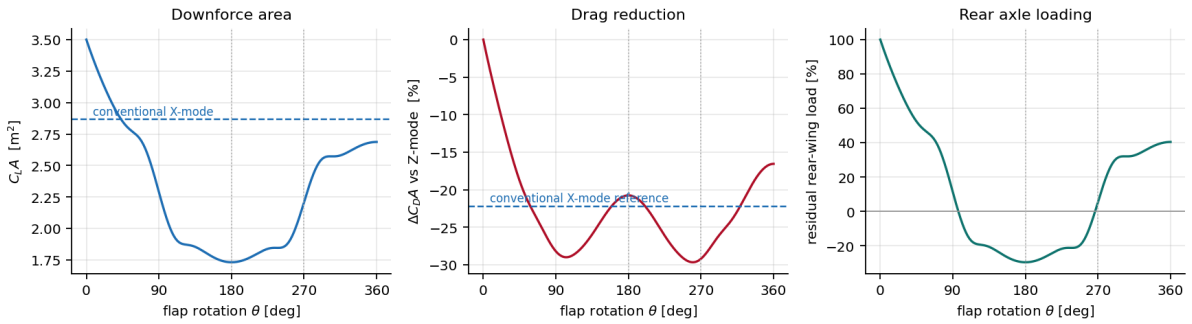


Figure 1. Whole-car aerodynamic state through the rotation cycle. Downforce area, drag reduction and residual rear-wing load are shown against rotation angle, with the conventional X-mode state marked as a reference level because it does not lie on the rotation locus.

This rephrases the function of this mechanism. It is not for the purpose of inverting the wing, but to move the flap out of the way from the mainplane on return to a streamwise position, providing both a large gap and close to zero incidence at the same time, a feat a hinged flap cannot achieve, as gap and incidence are mechanically linked. This is illustrated in the trade-off envelope in Figure 2; the 270° state is found in a region of the drag-downforce plane that is not possible to actuate by conventional means. At 180°, the state is inverted – it is not the goal; it is a transition that should be crossed as fast as possible.

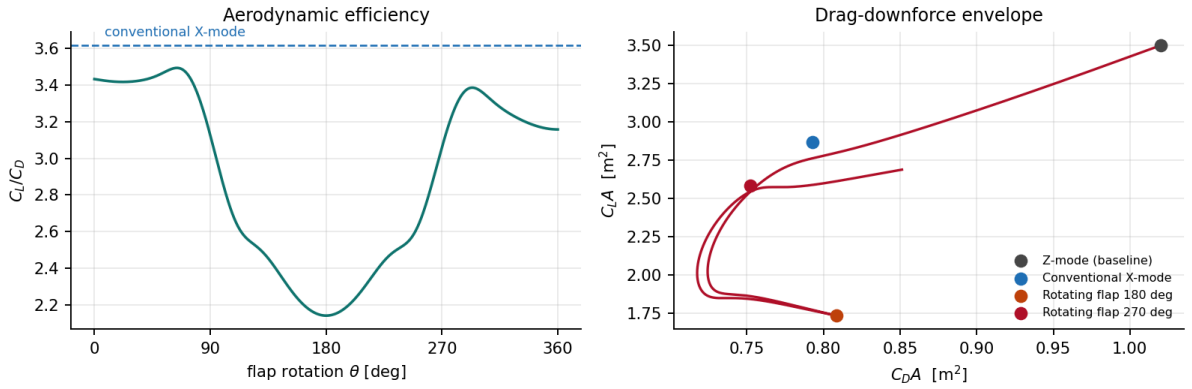


Figure 2. Aerodynamic efficiency through the rotation and the resulting drag-downforce envelope. Points toward the lower left of the envelope are unreachable by a hinged flap.

7.2 Drag characteristics

The aerodynamic loads as functions of velocity are shown in Figure 3. The 270° rotating flap can eliminate around 2.9 kN of drag at 340 km/h as compared to the Z-mode, while a conventional flap can only eliminate 2.4 kN of drag. Thus, the "incremental" advantage of the rotating mechanism is about 0.5 kN at the "terminal velocity" (true, but one order of magnitude below the advantage of having active aerodynamics all the time).

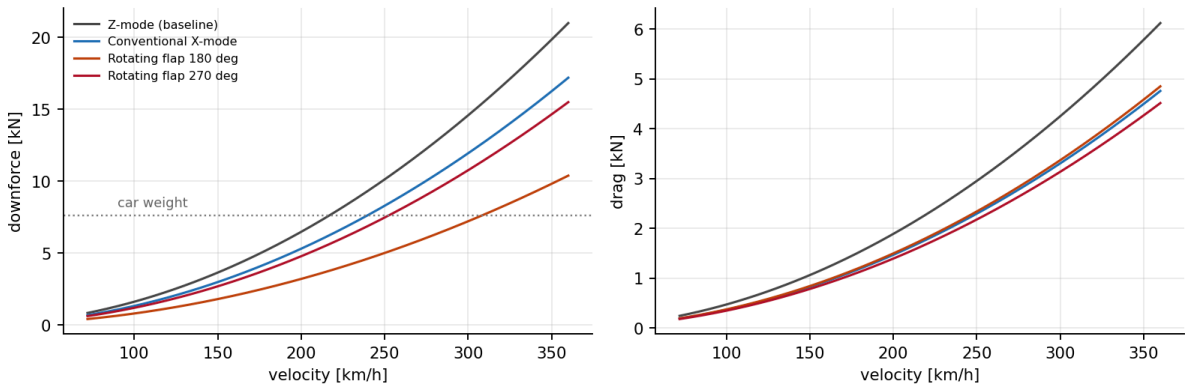


Figure 3. Downforce and drag against velocity for each configuration. The car weight reference line indicates the speed at which aerodynamic load exceeds vehicle weight.

A finding relevant to mechanism design that emerges from the archetype study in Section 7.5 is that the slot gap ratio (Gp) has a negligible effect on the whole-car drag coefficient (Cx) when changing the gap ratio from 0.62 to 0.78. When the mainplane is completely stalled, it is just about impossible to obtain any more separation from the flap, since the remaining drag is bluff-body pressure drag, which cannot be taken away by any additional flap separation. The aerodynamic return of aggressive travel is near zero; a large part of the risk assessment to follow is centred around this.

7.3 Lift-to-drag ratio

The aerodynamic efficiency (C_LA/C_DA) is 3.43 in Z-mode, becomes slightly increased to 3.62 in the conventional X-mode flap, and reverts back to 3.43 in the 270° flapped mode, but drops to 2.14 in the 180° inverted mode. But efficiency is not a good figure of merit for a mode-switching device. Z-mode (Maximum C□A at tolerable drag) vs X-mode (Minimum C_DA with acceptable load at the back for safe braking). It's not just the ratio, but the transition time between the states, and they're treated as performance variables, not mechanical details in this section, because of that.

7.4 Lap performance and Circuit Gilles-Villeneuve dependence

Table 2 summarises circuit characteristics and modelled outcomes; Table 3 reports lap time deltas against the Z-mode baseline.

Circuit	Length (m)	Corner fraction	Deployed fraction	Baseline lap (s)	v_max base (km/h)	v_max rotating (km/h)
Spa-Francorchamps	7004	0.159	0.727	99.604	327.3	340.6
Silverstone	5891	0.227	0.659	88.304	327.1	340.1
Circuit Gilles-Villeneuve	4361	0.146	0.655	74.945	326.9	339.5

Circuit	Length (m)	Corner fraction	Deployed fraction	Baseline lap (s)	v_max base (km/h)	v_max rotating (km/h)
Hungaroring	4381	0.205	0.571	80.400	327.1	340.1
Monaco	3337	0.761	0.060	77.989	294.0	294.9

Table 2. Circuit characteristics and baseline simulation outputs.

Circuit	Conventional X-mode	Rotating 180°	Rotating 270°	Advantage over conventional	Δv_max vs Z-mode baseline (km/h)
Spa-Francorchamps	−1.442	−1.422	−1.719	−0.277	+13.3
Silverstone	−0.938	−0.925	−1.114	−0.176	+13.0
Circuit Gilles Villeneuve	−0.648	−0.630	−0.768	−0.120	+12.7
Hungaroring	−0.541	−0.525	−0.641	−0.101	+13.0
Monaco	−0.031	−0.029	−0.036	−0.005	+0.9

Table 3. Modelled lap-time differences, in seconds, relative to the Z-mode baseline at nominal recovery times. Negative values indicate a reduction in lap time and therefore a faster simulated configuration. The "Advantage over conventional" column is calculated as t_rotating−t_conventional; consequently, a negative value indicates that the rotating configuration is faster. In the surrounding prose, the absolute magnitude of this difference is described as the lap-time advantage. The value of −0.277 s in the "Advantage over conventional" column corresponds to a 0.277 s lap-time advantage for the rotating configuration.

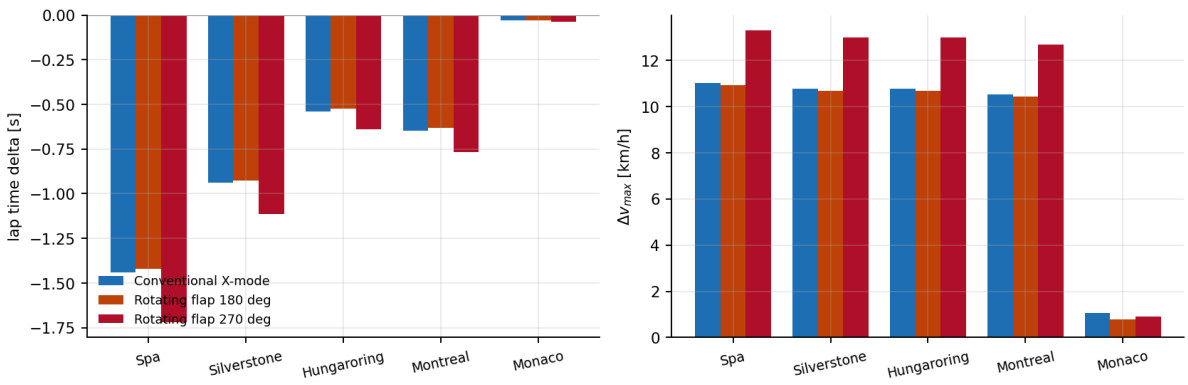
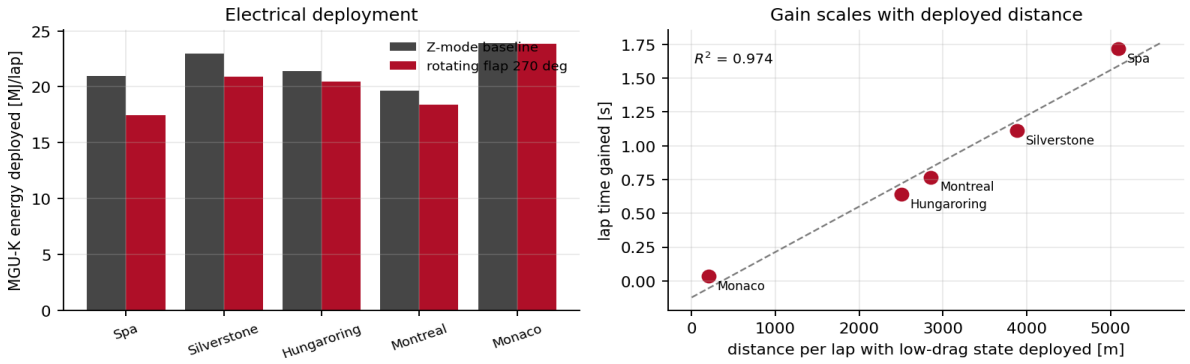


Figure 4. Lap time and top speed effects by circuit. The rotating 180° configuration performs comparably to or worse than a conventional flap on every circuit.

This 270° rotation gives a virtual lap-time benefit of 0.277 s at Spa-Francorchamps, 0.176 s at Silverstone, 0.120 s at Circuit Gilles-Villeneuve, 0.101 s at the Hungaroring and 0.005 s at Monaco compared to the standard X-mode flap configuration. The effect, therefore, is highly dependent on the circuit and is highest in circuits with long deployment zones. The short straights allow very little sustained use of the low drag configuration, which makes the performances of the various active-aerodynamic configurations converge, as is the case in Monaco. The modelling shows a maximum velocity of 340.6 km/h at the rotating configuration, while the conventional X-mode is around 338.4 km/h and the Z-mode baseline is 327.3 km/h.

The direction of the device is almost linear in the distance per lap over which the low-drag state is deployed (Figure 6, $R^2 = 0.974$), and there is no significant cornering contribution in the mechanism. The correlation is much weaker when there is a correlation against the deployed fraction of lap ($R^2 = 0.717$) as expected – it is not a benefit per lap fraction but a benefit per metre of lap that has been used. The electrical consequences of the rotating-flap configuration across the analysed circuits are shown in Figure 5 with the deployment reduced by 3.49 MJ per lap compared to the baseline, whilst a conventional flap would only be 2.86 MJ per lap. This energy saving could prove to be more important than the lap time itself, given that one of the biggest constraints of the 2026 formula will be deployment energy, with the resulting freed-up budget going to other parts of the lap.



Figures 5 and 6. Electrical deployment energy by circuit and configuration, and the relationship between lap time gain and the distance per lap spent in the low-drag state.

The decomposition of the gain (Figure 7) reveals that 91 % of the benefit of the Spa is realized in the deployment zones just inside the Spa and 9 % of the benefit is carried into the next corner as an entry speed. The device has nothing to do with better corners; it's about better arrivals.

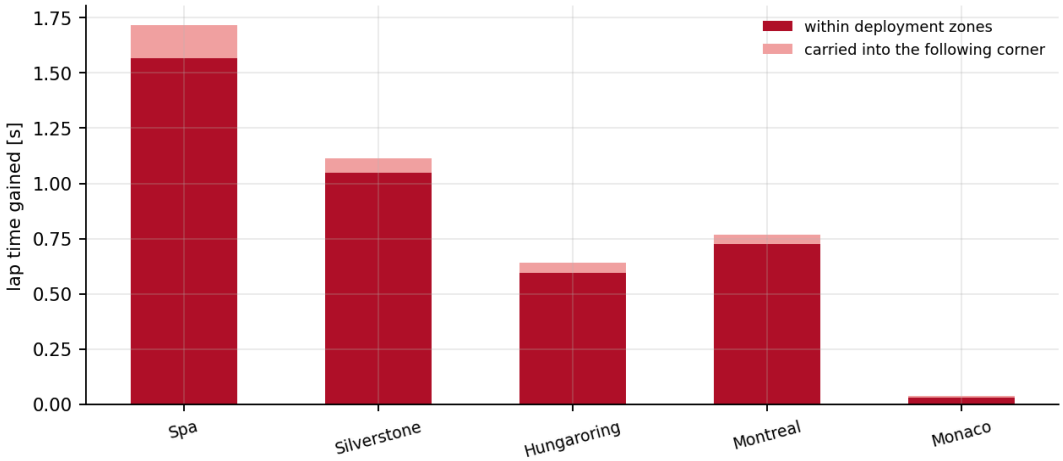


Figure 7. Decomposition of the lap time gain into time gained within deployment zones and time carried into the following corner.

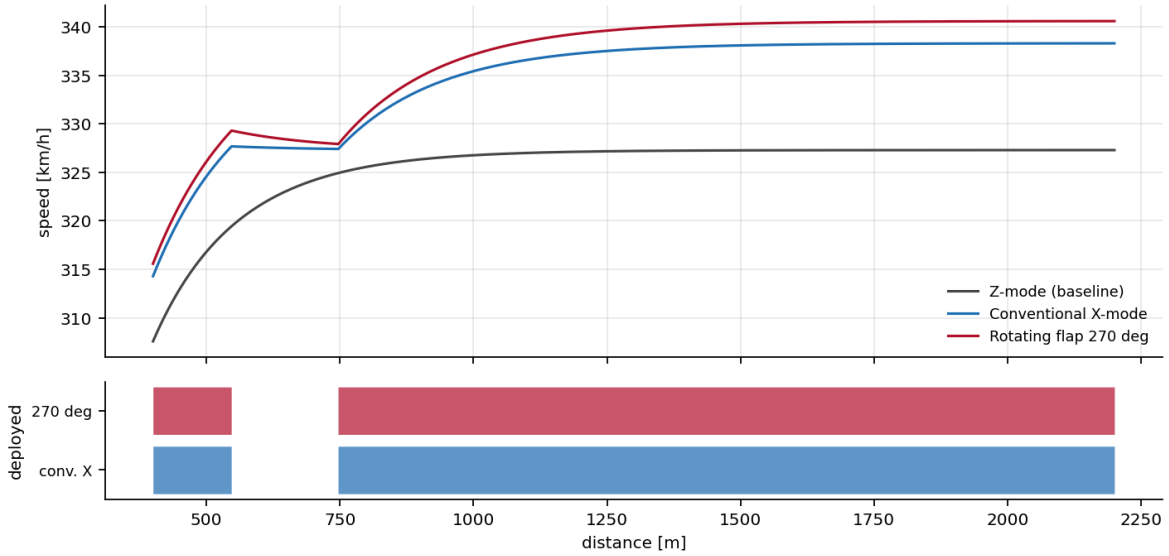


Figure 8. Velocity traces through Eau Rouge, the Kemmel straight and the approach to Les Combes, with deployment state shown below. The rotating configuration reaches 340.6 km/h against 338.4 km/h for a conventional flap and 327.3 km/h for the passive baseline.

7.5 Recovery time, stability and mechanism archetypes

The most important outcome of the study is the downforce recovery time. Using a higher τ (100 – 500ms) won't cost a lot in lap time (8 – 17ms). It's geometric - If the driver expects to be able to do this, he loses the low-drag property of the mechanism over $v \cdot \tau$ metres, and at 92 m/s, he has lost about 46 metres of a 1300 metre straight even with a 500 ms mechanism.

The modelled saturation of the rear axle at brake application increases in the same range between 1 % and 57 % (Table 4).

Recovery time τ (ms)	Restored fraction	Stability margin SM	P(SM < 1)	P(τ > 400 ms limit)
156	0.950	1.073	0.1 %	0.0 %
212	0.950	1.073	0.1 %	0.0 %
306	0.918	1.054	1.3 %	7.4 %
400	0.876	1.021	22.4 %	49.1 %
475	0.832	0.994	56.9 %	81.9 %
550	0.790	0.969	83.8 %	95.9 %

Table 4. Stability margin and excursion probability at brake application into Les Combes (340 km/h approach). The transition is a threshold rather than a gradient, occurring where τ exceeds the driver's anticipation budget.

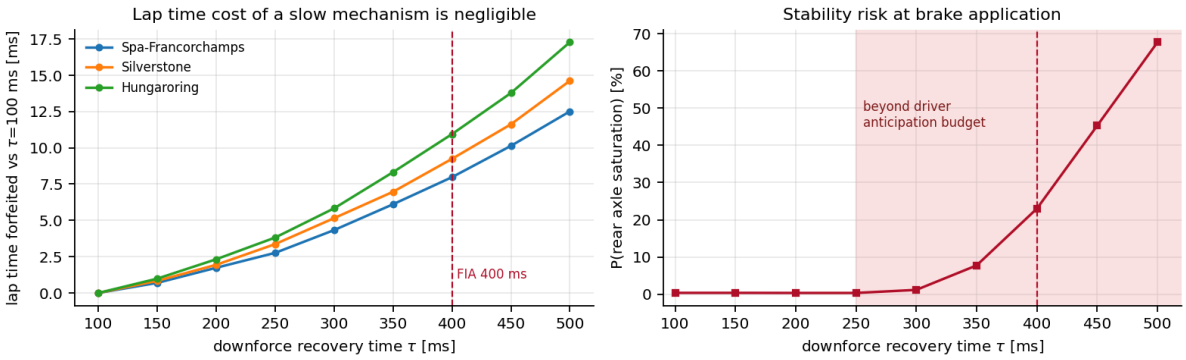


Figure 9. Lap time forfeited and stability risk incurred as functions of recovery time. The asymmetry between the two panels is the study's principal safety finding.

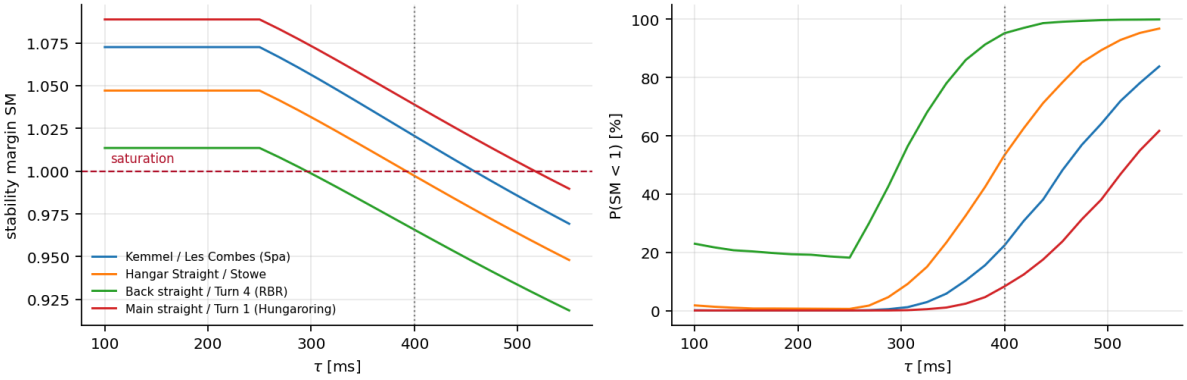


Figure 10. Stability margin and rear-axle saturation probability across four high-speed braking zones. Faster approaches with greater approach curvature saturate earlier.

Table 5 is applied to four mechanism archetypes, based on slot gap and recovery time. The archetypes are parametric, not hardware; the only public difference between the 2026 implementations is the placement of the actuators: endplate vs central pod, which suggests that there is a possibility that the travel and rate achievable by each are limited.

Archetype	g/c	τ (ms)	ΔC_D (%)	Gain over conventional (s)	P(saturation)	P(τ > 400 ms)
A - endplate, compact rotation	0.62	220	−26.2	−0.277	0.3 %	0.0 %
B - central pod, maximal gap	0.78	420	−26.6	−0.297	37.3 %	59.8 %

Archetype	g/c	τ (ms)	ΔC_D (%)	Gain over conventional (s)	P(saturation)	P(τ > 400 ms)
C - central pod, constrained travel	0.66	250	−26.4	−0.285	0.3 %	0.4 %
D - inverted, arrested at 180°	0.62	300	−20.7	+0.022	33.3 %	6.0 %

Table 5. Mechanism archetypes evaluated at Spa-Francorchamps. Archetype B buys 0.020 s over archetype A while raising saturation probability from 0.3 % to 37.3 %.

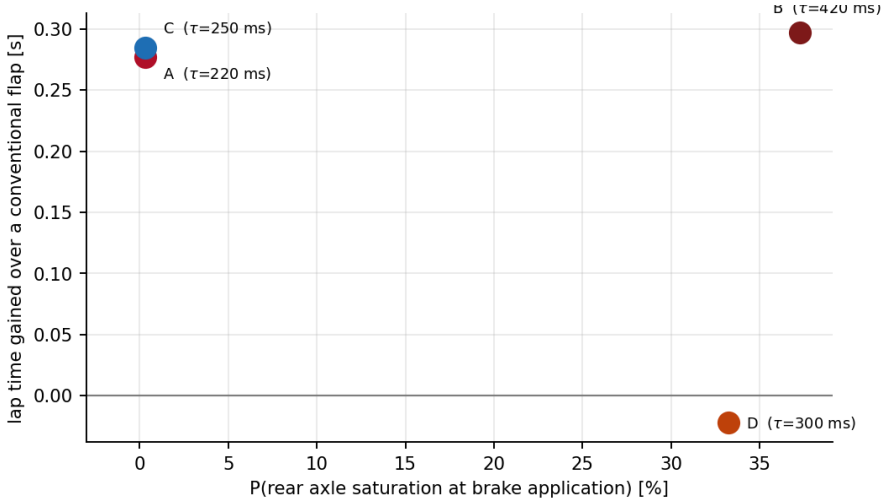


Figure 11. Lap time gained over a conventional flap plotted against rear-axle saturation probability for each archetype. The aggressive configuration occupies the worst region of the plane.

The comparison and contrast of the two archetypes is clear. Archetype B, aiming for a maximal gap and at the same time taking 420 ms to recover, gains 0.020 s in comparison to Archetype A, which is about two hundredths of a second, whilst simultaneously increasing the saturation probability from 0.3 % to 37.3 % and surpassing the FIA recovery limit on 59.8 % of deployments. The inverted variant of Archetype D, which was arrested, is 0.022 s slower than the conventional flap at 33.3 % saturation probability, and for which there is no rational design.

Two consequences follow. First off, it's not about corner entry; it's about braking at the end of long straight lines at high speed, which is the signature of the more aggressive variants. Second, and more alarming, a development programme that aims only at the lap time gets hardly any gradient on a perilously slow mechanism. The constraint should be based either on stability analysis or regulation. This gives a physical basis for the need for the FIA's 400ms recovery limit: It is working that competitive pressures would not.

7.6 Uncertainty and sensitivity

The 8 parameters were propagated through Monte Carlo analysis (n = 300 samples per circuit) and the results with intervals of 95 % are shown: At Spa: advantage of the rotating flap over a conventional flap of −0.276 s [−0.363, −0.201] and at the Hungaroring: advantage of the rotating flap over a conventional flap of −0.100 s [−0.132, −0.074]. The advantage is positive in 100 % of the samples on both of the circuits; therefore, the sign of the result is not sensitive to the parameters, but its magnitude is.

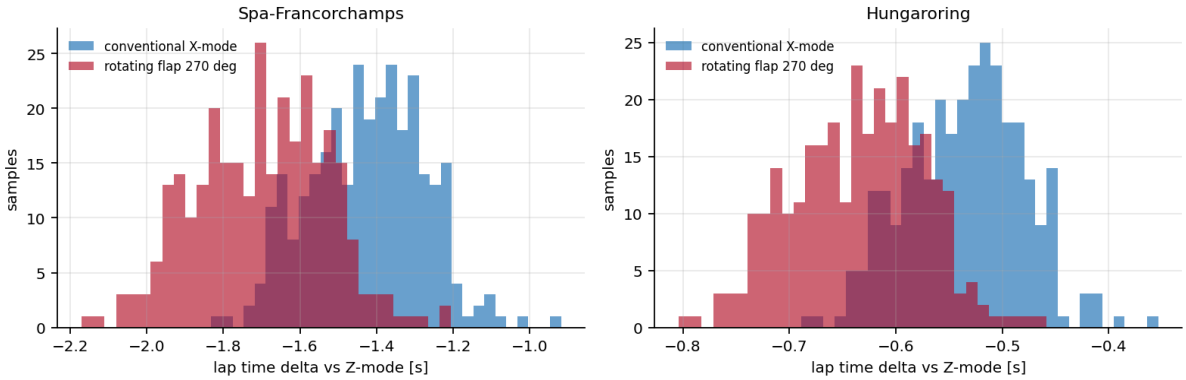


Figure 12. Monte Carlo propagation of aerodynamic and vehicle parameter uncertainty.

Running the sensitivity analysis through the standardised procedure, the mainplane drag floor and the contribution of the rear wing to the vehicle drag are found to be dominating. Both relate to the amount of bluff-body drag that persists past the stall; a hybrid RANS-LES computation or a wind tunnel campaign could measure this directly. Anyone who wishes to challenge the results reported shall start there.

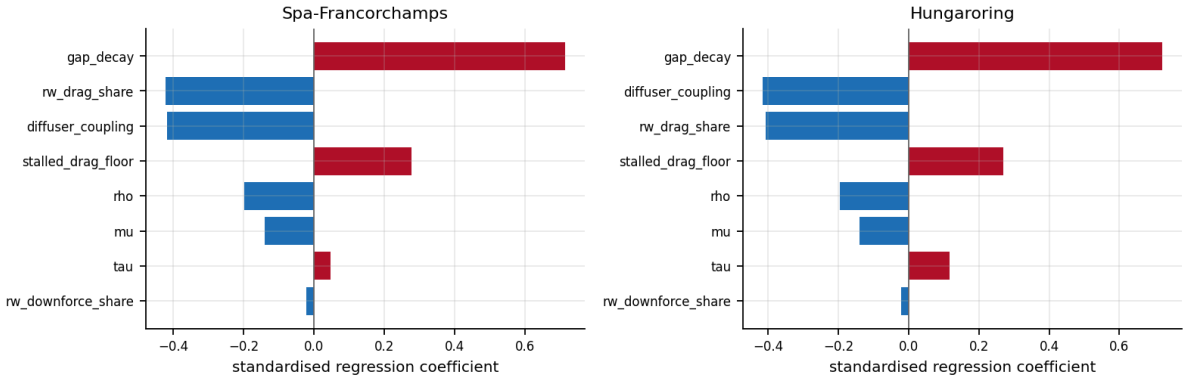


Figure 13. Standardised sensitivity of the rotating flap's advantage over a conventional flap. Positive coefficients erode the advantage.

7.7 Statistical framework for empirical validation

More care needs to be taken when testing these predictions against session data, as is often done in technical commentary. The impact of fuel load on raw lap time is an order of magnitude higher than the effect, at 0.032 s/kg, which contributes up to 3 s over a stint; compound differences contribute 0.4-0.8 s

over a stint; tyre age contributes 0.02-0.12 s/lap; and track evolution contributes 1-2 s over a weekend. The effect tested is in the range of 0.1-0.3 s. As well as this, the assignment is also not random: aggressive setups are used on circuits of low downforce in good conditions, with possibly almost all of the confounder parameters being correlated by the choice of wing.

The benefits of not doing so can be quantified by simulation. An estimator that assumes that each lap is an independent observation (as a per-session delta table assumes) had a coverage of 39.5 % against a nominal 95 % on 200 synthetic datasets, each with a known −0.15 s effect, with intervals half their correct size. A cluster-robust specification, adjusting for fuel, compound, tyre age and track temperature, resulted in a coverage of 91.0 %.

Estimator	Interval coverage (nominal 95 %)	Mean interval width (s)
Naive, laps treated as independent	39.5 %	0.269
Cluster-robust, adjusted	91.0 %	0.514

Table 6. Interval coverage by estimator across 200 simulated datasets with a known effect.

Four design suggestions are given below. Near-instantaneous (speed trap) and direct (straight-line) measurements of drag should take precedence, with the inclusion of a slipstream indicator (otherwise the low-drag configuration would be used disproportionately in clean air, and the indicator would bias the estimate badly). Wherever possible, within-session contrasts (two cars of one team are run concurrently in different configurations) should be used. The random-intercept mixed model should be used instead of cluster-robust ordinary least squares because the latter is better suited since the configuration of the wings is fixed across sessions and the random intercept for a session is competing with the random intercept for the treatment in the same variance. Last but not least, power should be reported: This means that it takes about 80 driver-sessions to resolve an effect at 80 % power, which is why a few sessions are insufficient to resolve the question.

The weakness of any such design is the lack of presence of wing configuration in any of the timing data sets, and it would need to be manually coded based on photographs for each car and each session. This coding table should be published as an addendum; the author identified, and unconfirmed sessions indicated as missing.

8. COMPARATIVE REVIEW OF EXISTING WING STUDIES

The published literature on the aerodynamic aspects of Formula One can be subdivided into three classes, none of which has dealt directly with the present problem.

A look at regulatory and historical reviews reveals the relationship between technical rules and aerodynamic development and how aerodynamic development focuses on each restriction instead of saving on it. These only give some context, but aerodynamic states are no longer allowed in the 2026 formula (Wright 1982; Katz 2019; Federation Internationale de l'Automobile 2026c).

Computational analyses of individual wing components and whole vehicles are used to validate the numerical methods in Section 5 and to offer validated correlations for multi-element assemblies in attached flow. They are very limiting in this problem, because the performance-critical part of their operation is very steady-state while the safety-critical part of the operation is in the transition between steady states in flow regimes, which are massively separated from each other, but the device studied here is in massively separated flow during the performance-critical phase and in the attached regime during the safety-critical phase. There is little published validation data available for stalled multi-element wing assemblies in ground effect (Spalart et al. 1997; Buscariolo et al. 2022).

The closest analog and useful result of DRS-era research are studies on AR, which showed that a reduction in total drag of about 10-12 % is achievable with the opening of flaps, at least for the DR. The three distinct differences of the 2026 case with respect to the direct transfer made to date are: drag reduction is not just on the rear wing, but also on the underbody; the front wing is not a passive device, its centre of pressure is itself a dynamic control variable; and the deployment taper for the power unit introduces a feedback where, in every pre-2026 analysis, it was not present.

For the particular device, the material available is journalistic and not scholarly. It confirms the existence of a mechanism, its timelines and the location of actuators in a reliable fashion and provides performance data in an unreliable way, as explained in Section 1.1. This paper is filling the gap where no published treatment has yet been done to couple the aerodynamic state of a large rotation flap with vehicle dynamics when braking, the true engineering challenge of this concept.

9. DISCUSSION

The results change the outlook of the rotating flap concept in three ways:

The purpose of the mechanism is NOT inversion. The 180° flip results in less drag reduction when driving rear wing load negative (RWLN), and the oft-repeated statement that the inverted profile creates useful positive lift, on this model, is a misreading of a disadvantage as a benefit. Any section with a negative camber angle greater than the minimum found at the minimum safe incidence is considered to be bluffed and generates the same amount of high-pressure drag, as it removes the rear-axle load that is necessary for a stable braking event. The simultaneous combination of a large slot gap and near-zero incidence, which is possible near 270°, is what the mechanism provides that a hinged flap does not. Gap and incidence are mechanically coupled in a hinged flap, but are decoupled in a rotating flap. It's the entire engineering aspect of the concept, and it equates to approximately four per cent of the whole car drag.

The size of the advantage is small and often exaggerated. Against the regular 2026 X-mode flap, the modelled gain is 0.277 s at Spa, 0.101 s at the Hungaroring and the top speed is 2.3 km/h. These are certainly competitive-looking margins, but the bulk of the performance, which was credited to the concept in the secondary coverage, is just the effect of active aerodynamics, which is available to all the cars on the grid. Careful comparison should be made with a conventional X-mode flap, and many of the comments made to date do not differentiate between the two.

There is no aerodynamic constraint, just a time constraint. The widest implications are the result of this finding. The optimisation landscape a team is put in is active misoptimising: lap simulation, the main development tool, gives virtually no penalty for a dangerously slow mechanism. An aggressive travel gain in aerodynamics is almost zero after the mainplane has stalled, and this applies even in principle. An optimization programme that is optimizing the metric it can measure will end up in a configuration where the hazard is only in a domain that it does not simulate. This is a particular case of a general trend in safety-critical engineering, and may be the best evidence for the FIA's 400ms recovery limit being a true limit, not an arbitrary one. The limit has a role that other competitive forces don't have.

These conclusions are based on a model that must be asserted, not measured, and given as tentative predictions that can be tested. The bluff-body drag, the dominant sensitivity, is directly measurable, and a transient computation or a tunnel campaign that addresses the bluff-body drag would either confirm or refute the quantitative claims presented here.

10. CONCLUSION

In this study a coupled aerodynamic, quasi-steady lap-simulation model and a vehicle-stability model were developed to study large-angle rear-wing rotation under the 2026 Formula One active-aerodynamics regulations. Due to the nature of the Ferrari aerodynamic and actuator information, this analysis is here explicitly parametric and the numbers presented as a prediction of model performance and not measured SF-26 performance.

Three main findings come to the fore. The first is that the aerodynamic optimum of the rotating flap is not at 180°, but in the vicinity of 270°. The fully inverted configuration has a smaller drag reduction than the conventional X-mode flap (−20.7% vs. −22.3%), a smaller rear-wing load residual (−29.5% vs. 53.6% for the conventional configuration), and a more forward aerodynamic balance reaching 88.9% compared with 44.0% for the conventional flap. The flap is fully open and in near streamwise incidence at 270° for the largest drag reduction of −26.2% with a positive residual load of 32.8% at the rear. However, the most important advantage of the mechanism is to decouple the flap incidence from the slot gap, rather than creating an inverted-wing state. The main aerodynamic benefit of the rotating system over wing inversion is actually the combination of a large slot gap with a near streamwise flap incidence that is not easily obtained with a conventional hinged flap.

Second, the predicted improvement in performance over a conventional X-mode flap is actually there but small. The overall gain is around 0.28s at Spa-Francorchamps, 0.18s at Silverstone, 0.12s at Circuit Gilles-Villeneuve, 0.10s at the Hungaroring and <0.01s at Monaco. The rotating setup gives around 2.2 km/h extra top speed compared to the normal X-mode setup, while it is around 13.3 km/h extra compared to the Z-mode basic configuration. Monte Carlo simulations show that the predicted direction of the lap-time advantage is fairly stable with respect to the tested parameter uncertainty but the exact value is model dependent.

Thirdly, the time to recover from downforce is not a performance factor but more of a safety consideration. A small penalty in lap time is seen on increasing recovery time, whereas the modelled probability of having the rear-axle saturated during high speed braking increases rapidly as the recovery

time is increased. This means that there's not much competitive optimisation pressure on a team to avoid a slow mechanism based on lap time. For the purpose of the present model, this result gives a physical basis to impose an external constraint on the recovery time like the one imposed by the FIA of 400 ms.

The quantitative results depend on assumptions about the drag of the bluff-body, the contribution to total vehicle drag of the rear wing, the coupling between the wing and the diffuser, the actuator dynamics and the flow-reattachment behaviour. To validate the model, then, data from transient CFD, wind-tunnel force measurement and condition-controlled track data are necessary. However, the analysis suggests that the main engineering issue to consider for a large-rotation active rear wing is not whether it will result in an extremely low drag, but whether a sufficiently large slot gap can be obtained while retaining a fast and stable aerodynamic recovery prior to high-speed braking.

11. FUTURE PERSPECTIVES

The best thing that can be done next is a transient computational study. The results here are based on quasi-static aerodynamic states linked by an assumed first-order recovery lag, but the process is actually hysteretic – flow reattachment does not follow separation in reverse, and the time for the recovery of circulation can be significantly longer than mechanical travel time. A moving-mesh or overset hybrid simulation of the closing transient (RANS-LES) that resolves the closure time would better resolve whether the closing time is set by the actuator or flow and would answer the question of whether the problem of safety is achievable by faster hardware or not.

In practice, the key parameter is transient force measurement on a 60 % scale model having working internal actuation that is sampled at a sufficient rate to capture the recovery event, together with pressure-sensitive paint to verify the recovery of flow along the reversed profile. The mainplane drag floor, known to be the primary uncertainty, is not assumed but rather measured.

In addition, the model could be extended in two ways: a transient vehicle model that includes pitch and heave responses at modes switch-on and switch-off and the explicit inclusion of front-rear synchronisation, because the excursion of the centre-of-pressure is a function of the difference between the front mode and rear mode switch-on times rather than of either alone.

The approach outlined in Section 7.7 should be applied to the data collected from the sessions – the speed trap measurements should be the primary outcome, and a published configuration coding table should be used. Lastly, the regulatory issue raised in Section 9 deserves further consideration as a standalone issue: When a performance metric is not sensitive to a safety-critical parameter, there is nothing that the governing body can do that a competitor would have an incentive to do; it would be helpful for the governing body to be aware of such situations in advance for use in regulating motorsports in general.

Author's contributions: Vedant Katira conceptualised the study, carried out simulations, analysed data, wrote and corrected the manuscript.

Acknowledgement: I would like to thank my parents and school teachers for their help and support in completing this research project.

Conflict of interest: There is no potential conflict of interest to disclose.

Funding information: No funding information to disclose.

REFERENCES

Katz, Joseph. 2006. "AERODYNAMICS of RACE CARS." *Annual Review of Fluid Mechanics* 38 (1): 27–63. https://doi.org/10.1146/annurev.fluid.38.050304.092016.

Zhang, Xin, Willem Toet, and Jonathan Zerihan. 2006. "Ground Effect Aerodynamics of Race Cars." *Applied Mechanics Reviews* 59 (1): 33–49. https://doi.org/10.1115/1.2110263.

Spalart, P. R., W. H. Jou, M Strelets, and S. R. Allmaras. 1997. "Comments on the Feasibility of LES for Wings, and on a Hybrid RANS/LES Approach." *Advances in DNS/LES*, January 1. https://www.researchgate.net/publication/236888805_Comments_on_the_Feasibility_of_LES_for_Wings_and_on_a_Hybrid_RANSLES_Approach.

Soso, M D, and P. A. Wilson. 2006. "Aerodynamics of a Wing in Ground Effect in Generic Racing Car Wake Flows." *Proceedings of the Institution of Mechanical Engineers, Part D: Journal of Automobile Engineering* 220 (1): 1–13. https://doi.org/10.1243/095440705x69632.

Buscariolo, Filipe F., Julien Hoessler, David Moxey, et al. 2022. "Spectral/Hp Element Simulation of Flow Past a Formula One Front Wing: Validation Against Experiments." *Journal of Wind Engineering and Industrial Aerodynamics* 221 (February): 104832. https://doi.org/10.1016/j.jweia.2021.104832.

Guerrero, Alex, and Robert Castilla. 2020. "Aerodynamic Study of the Wake Effects on a Formula 1 Car." *Energies* 13 (19): 5183. https://doi.org/10.3390/en13195183.

Ehirim, O. H., K Knowles, and A. J. Saddington. 2018. "A Review of Ground-Effect Diffuser Aerodynamics." *Journal of Fluids Engineering* 141 (2). https://doi.org/10.1115/1.4040501.

Katz, Joseph, and Lee Dykstra. 1992. "Effect of Wing/Body Interaction on the Aerodynamics of Two Generic Racing Cars." *SAE Technical Paper Series* 1 (February). https://doi.org/10.4271/920349.

Lau, Chia Sheng, and Sutthiphong Srigrarom. 2010. "Flow Field Around the Front Wing of Formula One Racing Car Model: BAR Honda 003 and MP4-21 Under Ground Effect." *International Journal of Aerodynamics* 1 (1): 72. https://doi.org/10.1504/ijad.2010.031703.

Abid, Muhammad, Hafiz Abdul Wajid, Muhammad Zohair Iqbal, Shayan Najam, Ali Arshad, and Ammad Ahmad. 2017. "DESIGN and ANALYSIS of an AERODYNAMIC DOWNFORCE PACKAGE for a FORMULA STUDENT RACE CAR." *IIUM Engineering Journal* 18 (2): 212–24. https://doi.org/10.31436/iiumej.v18i2.679.

Zhou, Shanwei, Edwin F. J. Overmars, and Jerry Westerweel. 2026. "An Accelerating Inverted Wing With Ground Effect: Downforce Measurement and Reconstruction." *Experiments in Fluids* 67 (6). https://doi.org/10.1007/s00348-026-04191-5.

Jowsey, L, and M Passmore. 2010. "Experimental Study of Multiple-Channel Automotive Underbody Diffusers." *Proceedings of the Institution of Mechanical Engineers, Part D: Journal of Automobile Engineering* 224 (7): 865–79. https://doi.org/10.1243/09544070jauto1339.

Soso, M D, and P. A. Wilson. 2008. "The Influence of an Upstream Diffuser on a Downstream Wing in Ground Effect." *Proceedings of the Institution of Mechanical Engineers, Part D: Journal of Automobile Engineering* 222 (4): 551–63. https://doi.org/10.1243/09544070jauto284.

Mariani, Francesco, Claudio Poggiani, Francesco Risi, and Lorenzo Scappaticci. 2015. "Formula-SAE Racing Car: Experimental and Numerical Analysis of the External Aerodynamics." *Energy Procedia* 81 (December): 1013–29. https://doi.org/10.1016/j.egypro.2015.12.111.
Menter, F. R. 1994. "Two-Equation Eddy-Viscosity Turbulence Models for Engineering Applications." *AIAA Journal* 32 (8): 1598–1605. https://doi.org/10.2514/3.12149.

Chatpattanasiri, C, K Bunpapong, M Sahastharachai, and B Puangkird. 2022. "Numerical Study and Design of Side-Diffusers for Formula-SAE Car." *Journal of Research and Applications in Mechanical Engineering* 10 (1). https://ph01.tci-thaijo.org/index.php/jrame/article/view/246797.

Laguna-Canales, Aldo Saul, Guillermo Urriolagoitia-Sosa, Beatriz Romero-Ángeles, et al. 2023. "Mechanical Design and Numerical Analysis of a New Front Wing for a Formula One Vehicle." *Fluids* 8 (7): 210. https://doi.org/10.3390/fluids8070210.

Castro, Xabier, and Zeeshan A. Rana. 2020. "Aerodynamic and Structural Design of a 2022 Formula One Front Wing Assembly." *Fluids* 5 (4): 237. https://doi.org/10.3390/fluids5040237.

Nebot, Eugeni Pérez, Antim Gupta, and Mahak Mahak. 2025. "Investigating the Impact of Structural Features on F1 Car Diffuser Performance Using Computational Fluid Dynamics (CFD)." *Mathematics* 13 (9): 1455. https://doi.org/10.3390/math13091455.

Katz, Joseph. 2019. "Aerodynamics in Motorsports." *Proceedings of the Institution of Mechanical Engineers, Part P: Journal of Sports Engineering and Technology* 235 (4): 324–38. https://doi.org/10.1177/1754337119893226.

Nath, Devang S., Prashant Chandra Pujari, Amit Jain, and Vikas Rastogi. 2021. "Drag Reduction by Application of Aerodynamic Devices in a Race Car." *Advances in Aerodynamics* 3 (1). https://doi.org/10.1186/s42774-020-00054-7.

Federation Internationale de l'Automobile. 2026c. "| Federation Internationale De l'Automobile." https://api.fia.com/regulation/category/110.

Wright, P. G. 1982. "The Influence of Aerodynamics on the Design of Formula One Racing Cars." *International Journal of Vehicle Design* 3 (4): 383–397. https://doi.org/10.1504/IJVD.1982.061285.